Received: 20 February 2023 | Revised: 10 April 2023 | Accepted: 19 April 2023

DOI: 10.1002/suco.202300134

ARTICLE

fib CEB-FIP WILEY

Experimental study on basic and drying creep for an alkali-activated slag concrete and comparison with existing creep models

Richard Caron[1,2] | **Ravi A. Patel**[1,2] | **Frank Dehn**[1,2]

[1]Institute of Building Materials and Concrete Structures (IMB), Karlsruhe Institute of Technology (KIT), Karlsruhe, Germany

[2]Materials Testing and Research Institute (MPA), Karlsruhe Institute of Technology (KIT), Karlsruhe, Germany

Correspondence
Richard Caron, Institute of Building Materials and Concrete Structures, Karlsruhe Institute of Technology (KIT), 76131 Germany.
Email: richard.caron@kit.edu

Funding information
Horizon 2020 Framework Programme, Grant/Award Number: 813596

Abstract

Slag is a by-product of the steel industry that can be activated using alkali solutions to form concrete. This study presents new experimental results of basic and drying creep behavior of alkali-activated slag (AAS) concrete. Different parameters affecting creep such as loading age, sample size and creep stress-strength ratio were varied for experimental studies. The results show that the basic creep of AAS concrete is higher than that of ordinary Portland cement (OPC) concrete. The drying creep of AAS is lower than for OPC and this could be explained by a higher internal drying during the activation of slag. The experimental results were used to check the applicability of two existing engineering models, the *fib* MC 2010 and the B4s model, for AAS concrete. It was found that both models could be extended to predict the basic creep of AAS concrete. For drying creep, the B4s could better capture the creep behavior. For the *fib* MC 2010, a new formulation for drying creep would be required.

KEYWORDS

alkali-activated slag, B4s model, creep, *fib* MC 2010

1 | INTRODUCTION

In the past decades, new types of binders have been extensively studied in order to propose alternatives to ordinary Portland cement (OPC). Among them, the activation of slag, fly ash and metakaolin using alkali solutions to form a hardening matrix seems to be a promising approach. Such binder systems are termed as alkali-activated materials (AAMs).[1] In comparison to OPC, alkali-activated slag (AAS) contains higher amounts of silicon and aluminum oxides and less calcium oxide.[2] This difference in oxide content induces different reaction products. However, several studies showed that the compressive strength of this material is comparable to cement-based systems.[3–5] In addition, AAS was proven to have a better resistance to chloride ingress and a lower permeability than cement-based systems.[6,7] Thus, the use of AAS for producing concrete could be a key to increasing the durability and lifespan of structures for certain exposure conditions.

Both OPC and AAS concrete structures experience deformations. If they are excessive, these deformations endanger the safety of the structures and thus reduce their service life. They can occur in loading-free conditions or under sustained load applied on the concrete. In the latter case, the associated deformations are referred to as creep. For bridge structures, surfaces can become non-planar and affect their use[8] or show excessive

deflections.[9] Reactor containments are other examples of structures that undergo high strains under loading. These deformations must be predicted and controlled to reduce the formation of cracks.[10,11] It was also shown that creep can lead to an increase in carbonation[12] and chloride ingress.[13]

Basic creep is defined as the creep that takes place in sealed conditions, i.e. without moisture exchange with the surrounding environment. Drying creep is defined as the additional creep occurring with moisture exchange. Under constant load $\sigma(t) = \widehat{\sigma}$ (MPa) applied on the material at the age t_0 (d), the compliance function $J(t,t_0)$ (1/MPa) is defined as:

$$\varepsilon(t) = \widehat{\sigma} J(t,t_0), \tag{1}$$

where $\varepsilon(t)$ (−) is the strain at time t (d). To predict the strain evolution of cement-based concrete, the compliance function of Equation (1) has been modeled in the B3 model by Bazant and coworkers.[14,15] The B4 model extends and improves the B3 model.[16] It is a semi-empirical creep model based on the solidification theory for aging viscoelasticity and solidifying material.[16] It was first developed to predict the creep strain as a function of the mix design. However, a simplified model, the B4s model, has been developed in which the creep strain is expressed as a function of the characteristic compressive strength.

Another way to define creep strains is to use the experimental creep coefficient $\phi(t,t_0)$ defined as the normalized creep strain by the strain at loading:

$$\phi(t,t_0) = \frac{\varepsilon_{cc}(t,t_0)}{\varepsilon_{ci}(t_0)} = E_c(t_0) \cdot J(t,t_0) - 1, \tag{2}$$

where $E_c(t_0)$ is the modulus of elasticity of concrete at loading age. The *fib* MC 2010 is an empirical model that also predicts the creep strain from the characteristic compressive strength of concrete. This model is based on a modified definition of the creep coefficient:

$$\phi_{MC}(t,t_0) = \phi(t,t_0) \cdot \frac{E_{ci}}{E_c(t_0)}, \tag{3}$$

where ϕ_{MC} is the creep coefficient of the *fib* MC 2010 and E_{ci} is the modulus of elasticity of concrete at 28 days. This model was calibrated experimentally and is valid for creep loading lower than or equal to 40% of the compressive strength at loading age. For both *fib* MC 2010, B4 and B4s models, the basic creep and the drying creep are regarded as additive and independent.

Creep was also studied and compared with the previous engineering models for other binder types as recycled aggregate concretes[17] or alkali-activated fly ash.[18–20] Few studies have been made on the creep of AAS.[21–24] Humad et al.[24] proposed that the relative high creep could come from the increased presence of micro-cracks in the AAS matrix. Zhou et al. proposed an extension of the GL2000 model for AAS with sodium silicate.[21] However, no comparison with both *fib* MC 2010 and B4s models have been formulated so far.

In this study, new results of the creep behavior of AAS concrete are presented. Experiments on both sealed and unsealed conditions were performed. The influences of loading age, specimen diameter and creep stress-strength ratio on the creep behavior of this material were investigated. Two engineering models, namely the *fib* MC 2010 and the B4s model, were calibrated from the experimental results. These two models were originally developed for OPC concretes but they have been extended for other types of concrete. This study aims at examining whether they can be adapted to predict creep behavior of the AAS concrete.

2 | MATERIALS AND METHODS

2.1 | Materials

The slag used in this study was provided by the company Ecocem (Netherlands). Its oxide composition was determined with energy dispersive X-ray fluorescence (XRF) spectrometry with an M4 Tornado (Brucker GmbH Karlsruhe, Germany) (see Table 1). The activator used to make the slag react was a blend of commercial waterglass solution, commercial NaOH solution and tap water. The water glass was Betol 39 T, provided by Wöllner GmbH (Germany). It consists of 64%—mass of water, 8.2%—mass of Na_2O and 27.8%—mass of SiO_2. The NaOH solution had a 50% mass concentration of solid NaOH. The used alkali solution had an alkali dosage (n) equal to 5 (g Na_2O/100 g slag), a silicate ratio (M_S) equal to 0.5 (mol SiO_2/mol Na_2O) and a water/slag ratio w/s equal to 0.45 (kg/kg). This mix design is close to the mix design of the mix S3a of the RILEM round-robin test for alkali-activated concretes.[5,25] The generated concrete had a density of 2.25 kg/m^3. The mix design is summed up in Table 2.

2.2 | Methods

2.2.1 | Mixing procedure, casting and storage

The alkali solution was prepared 24 h in advance so that it reaches the temperature of the surrounding

TABLE 1 Chemical composition of the anhydrous slag.

Oxide	CaO	SiO_2	Al_2O_3	MgO	Fe_2O_3	Na_2O	K_2O	H_2S	Oth.
Mass (%)	38.8	36.3	12.8	8.0	0.6	0.3	0.6	1.0	1.6

TABLE 2 Mix design of the concrete.

Parameter	Unit	Value
w/s	(kg/kg)	0.45
n	(Na_2O g/100 g slag)	5.0
M_S	(SiO_2/Na_2O mol/mol)	0.5
Precursor content	(kg/m^3 of concrete)	450
Sand (0–2 mm)	(Vol-%)	40
Agg. (2–8 mm)	(Vol-%)	30
Agg. (8–16 mm)	(Vol-%)	30
Density	(kg/m^3)	2.25
Compressive strength	(MPa)	56

environment before being mixed with the slag. The dry ingredients were mixed for 30 s. The alkali solution was then added and the mixture was mixed for 1 min. After a resting time of 30 s, the mixture was mixed for 2 min. Cylindrical samples of 100 or 150 mm diameter and 300 mm height were cast. Additionally, cubes of characteristic size equal to 150 mm were cast. All the samples were de-molded after 24 h and covered with aluminum-butyl foil to prevent water loss. When needed, the sealing was removed at the corresponding age for exposure to drying t_s. The surfaces subjected to loading for concrete samples used for Young's modulus and creep tests were ground at an age of at least 6 days to have uniform contact with the loading plates.

2.2.2 | Mechanical tests on concrete samples

The compressive strength of concrete specimens was measured after 28 days with three cubes of characteristic size 150 mm, following the standard DIN EN 12390-3[26] where the samples were covered with plastic foil for the first 7 days and uncovered until the test day. The compressive strength measured with these cubes is given in Table 2 and is regarded as an intrinsic value of the mix design for this study. The ambient conditions were 20°C and 65% relative humidity. The Young's modulus and the compressive strength of cylinders were determined according to EN 12390-13[27] (method B) on six samples with the same geometry and the same curing conditions as the one used for creep tests before each creep measurement.

The deformations of concrete were measured with linear variable differential transformers (LVDTs) provided by the company Hottinger Brüel & Kjaer GmbH (Germany). Three LVDTs were placed at the center of each specimen and spaced at an angle of 120° on the sample. The gauge length for the measurement was 150 mm.

The creep setup is described in Figure 1. It consists of a hollow steel spring filled with hydraulic oil, a loading frame and a pressure pipe with the loading device. The hollow steel was connected to a pressure tank through a pipe filled with oil and nitrogen. After that the specimens equipped with the LVDTs were mounted on the loading frame, the above transverse was put on the spherical cap and fixed with a screw-nut system. Oil was then released from the pressure tank to reach the wanted value of pressure. Throughout the test, the pressure changes were recorded by an absolute pressure transducer P8AP (Hottlinger Baldwin Messtechnik GmbH).

Basic creep was studied for cylinders of 100 mm and 150 mm diameters for the same height of 300 mm with a loading age equal to either 7 or 28 days. Drying creep was always investigated with samples subjected to drying after 7 days. Three loading ages were investigated with specimens of 100 mm diameter: 7, 28 and 100 days. For the loading ages 7 and 28 days, the drying creep of specimens of 150 mm diameter was also measured. The sustained loads during creep experiments were always taken as a percentage of the compressive strength at loading age. For most of the experiments, the creep stress-strength ratio $R_{cr} = \frac{f_{cr}}{f_{cm(t_0)}}$ (%) was kept equal to 33%. Here, $f_{cm}(t_0)$ is the compressive strength at the loading age and f_{cr} is the sustained load during the creep test. With 100 mm diameter specimens, additional studies for R_{cr} equal to 20% and 60% were conducted for unsealed samples at a loading age of 28 days to understand the influence of R_{cr}. The experimental plan for creep tests is summarized in Table 3.

Parallel specimens were used to determine both basic shrinkage and drying shrinkage of the material with the same measuring tool as for creep, i.e., three LVDTs per specimen, without loading. Two replicates were used for each geometry (100 or 150 mm diameter) and each curing condition (always sealed, or sealed for 7 days and then unsealed). Shrinkage contribution was subtracted from the measurements on loaded specimens to obtain creep strains.

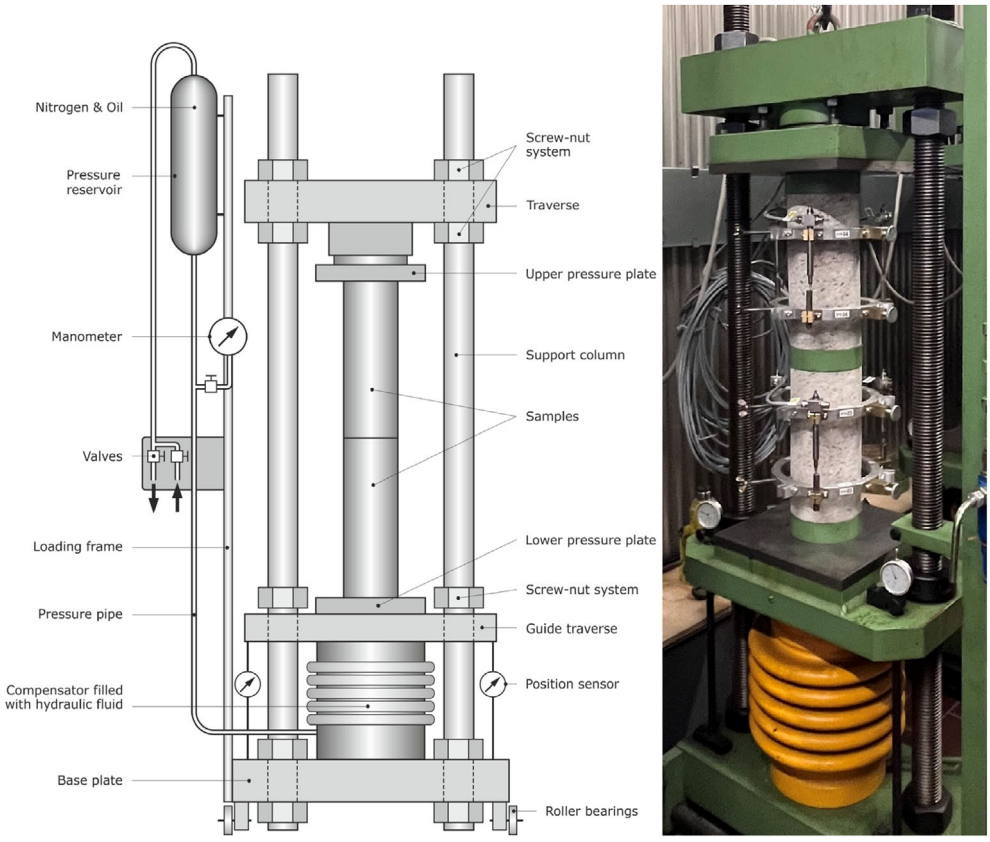

FIGURE 1 Experimental creep setup used in this study.

TABLE 3 Experimental plan for creep experiments.

Name	t_s	t_0	R_{cr}	d
Unit	days	days	%	mm
BC-7d-Ø100	n.a.	7	33	100
BC-28d-Ø100	n.a.	28	33	100
BC-7d-Ø150	n.a.	7	33	150
BC-28d-Ø150	n.a.	28	33	150
DC-7d-Ø100	7	7	33	100
DC-28d-Ø100	7	28	33	100
DC-7d-Ø150	7	7	33	150
DC-28d-Ø150	7	28	33	150
DC-100d-Ø100	7	100	33	100
DC-28d-Ø100-20%	7	28	20	100
DC-28d-Ø100-60%	7	28	60	100

Note: n.a stands for not applicable.

3 | MODELING OF THE CREEP BEHAVIOR OF CONCRETE

3.1 | Creep model based on the *fib* MC 2010

In the *fib* MC 2010, the total strain ε_c (μm/m) at a given time t (d) can be predicted by using:

$$\varepsilon_c(t) = \varepsilon_{ci}(t_0) + \varepsilon_{cc}(t) + \varepsilon_{cs}(t) + \varepsilon_{cT}(t), \quad (4)$$

where $\varepsilon_{ci}(t_0)$ (μm/m) is the initial strain at loading at t_0 (d), $\varepsilon_{cc}(t)$ (μm/m) is the creep strain for $t > t_0$, $\varepsilon_{cs}(t)$ (μm/m) is the shrinkage strain and $\varepsilon_{cT}(t)$ (μm/m) is the thermal strain.

Under the assumption that the applied stress σ_c (MPa) at time t_0 is below 40% of the compressive strength at $t = t_0$, the creep strain is expressed using the creep coefficient $\phi_{cc}(t, t_0)$ (−):

$$\varepsilon_{cc}(t, t_0) = \frac{\sigma_c(t_0)}{E_{ci}} \phi_{cc}(t, t_0) \quad (5)$$

E_{ci} (MPa) is the modulus of elasticity at the age of 28 days.

The creep coefficient is additively decomposed into the basic creep coefficient ϕ_{bc} (−) and the drying creep coefficient ϕ_{dc} (−):

$$\phi_{cc}(t, t_0) = \phi_{bc}(t, t_0) + \phi_{dc}(t, t_0), \quad (6)$$

ϕ_{bc} is predicted using the following function:

$$\phi_{bc}(t, t_0) = \beta_{bc}(f_{cm}) \cdot \beta_{bc}(t, t_0), \quad (7)$$

where

$$\begin{cases} \beta_{bc}(f_{cm}) &= \dfrac{1.8}{(f_{cm})^{0.7}} \\ \beta_{bc}(t,t_0) &= \ln\left(\left(\dfrac{30}{t_{0,adj}}+0.035\right)^2\cdot(t-t_0)+1\right), \\ t_{0,adj} &= t_{0,T}\cdot\left[\dfrac{9}{2+t_{0,T}^{1.2}}+1\right]^{\alpha}\geq 0.5 \text{ days} \end{cases} \quad (8)$$

f_{cm} (MPa) is the mean compressive strength at 28 days. $t_{0,T}$ (d) is the age of concrete at loading (constant in isothermal conditions). $t_{0,adj}$ (d) is the adjusted age at loading accounting for the type and maturity of concrete. α is a coefficient that depends on the strength class of cement: $\alpha=-1$ for strength class 32.5 N; $\alpha=0$ for strength classes 32.5 R and 42.5 N; $\alpha=1$ for strength classes 42.5 R, 52.5 N and 52.5 R.

$\phi_{dc}(t,t_0)$ is estimated using the following function:

$$\phi_{dc}(t,t_0)=\beta_{dc}(f_{cm})\cdot\beta(RH)\cdot\beta_{dc}(t_0)\cdot\beta_{dc}(t,t_0), \quad (9)$$

with

$$\begin{cases} \beta_{dc}(f_{cm}) &= \dfrac{412}{(f_{cm})^{1.4}} \\ \beta(RH) &= \dfrac{1-\dfrac{RH}{100}}{\sqrt[3]{0.1\cdot\dfrac{h}{100}}} \\ \beta_{dc}(t_0) &= \dfrac{1}{0.1+t_{0,adj}^{0.2}} \\ \beta_{dc}(t,t_0) &= \left[\dfrac{(t-t_0)}{\beta_h+(t-t_0)}\right]^{\gamma(t_0)} \end{cases}, \quad (10)$$

where

$$\begin{cases} \gamma(t_0) &= \dfrac{1}{2.3+\dfrac{3.5}{\sqrt{t_{0,adj}}}} \\ \beta_h &= 1.5\cdot h+250\cdot\alpha_{f_{cm}}\leq 1500\cdot\alpha_{f_{cm}} \\ \alpha_{f_{cm}} &= \left(\dfrac{35}{f_{cm}}\right)^{0.5} \end{cases}, \quad (11)$$

RH (%) is the relative humidity of the ambient environment. h (mm) is the notional size of the sample and corresponds to twice the ratio between the cross-section and the perimeter of the sample in contact with the atmosphere.

These functions were derived from experiments with OPC-based concrete. To extend this model to other types of concrete, four parameters were introduced in the revision of Eurocode 2[28]: ξ_{bc1} and ξ_{bc2} corresponding to basic creep, and ξ_{dc1} and ξ_{dc2} corresponding to drying creep. This approach was already used by Tosic et al.[17] to model the creep behavior of recycled aggregate concretes. The extended model is described as:

$$\phi(t,t_0)=\xi_{bc1}\cdot\phi_{bc}(t,t_0)+\xi_{dc1}\cdot\phi_{dc}(t,t_0), \quad (12)$$

and the additional parameters are introduced in:

$$\begin{cases} \widetilde{\beta}_{bc}(t,t_0) &= \ln\left(\left(\dfrac{30}{t_{0,adj}}+0.035\right)^2\cdot\dfrac{(t-t_0)}{\xi_{bc2}}+1\right) \\ \widetilde{\beta}_{dc}(t,t_0) &= \left[\dfrac{(t-t_0)}{\beta_h\cdot\xi_{dc2}+(t-t_0)}\right]^{\gamma(t_0)} \end{cases}, \quad (13)$$

If the values of the four parameters are taken equal to one, the original form is recovered. Comparing the above extension with that proposed in Tosic et al.[29] for basic shrinkage, the role of parameters ξ_{cbs1} and ξ_{cbs2} should correspond to the adaptation of the vertical scaling and the horizontal scaling, respectively. Vertical scaling refers to adapting the asymptotic behavior whereas horizontal scaling refers to controlling the rate of the creep. However, when using Equations (12) and (13), both parameters ξ_{bc1} and ξ_{bc2} have an influence on the asymptotic behavior of basic creep in Equation (13). Indeed, when $\left(\frac{30}{t_{0,adj}+0.035}\right)^2\cdot\frac{(t-t_0)}{\xi_{bc2}}>>1$:

$$\phi(t,t_0)\xrightarrow[\left(\frac{30}{t_{0,adj}}+0.035\right)^2\cdot\frac{(t-t_0)}{\xi_{bc2}}>>1]{}\xi_{bc1}\cdot\beta_{bc}(f_{cm})\cdot\ln\left(\left(\frac{30}{t_{0,adj}}+0.035\right)^2\cdot(t-t_0)\right)-\xi_{bc1}\cdot\beta_{bc}(f_{cm})\cdot\ln(\xi_{bc2}). \quad (14)$$

This causes difficulty in distinguishing the contributions arising from vertical and horizontal scaling for different types of concretes and different testing conditions. To avoid the above-mentioned inconsistency, the following extension is proposed for basic creep in this study:

$$\widetilde{\widetilde{\beta}}_{bc}(t,t_0)=\ln\left(\left(\frac{30}{t_{0,adj}}+0.035\right)^2\cdot(t-t_0)+1\cdot\xi_{bc2}\right). \quad (15)$$

In that case, the vertical scaling is only parameterized by ξ_{bc1} and the horizontal scaling is only parameterized by ξ_{bc2}. The inconvenient of the use of Equation (15) comes from the fact that the value at loading age ($t=t_0$) is not zero since $\widetilde{\widetilde{\beta}}_{bc}(t_0,t_0)=\ln(1\cdot\xi_{bc2})$.

3.2 | Creep model based on the B4s model

The B4s model predicts also the creep behavior of concrete taking the characteristic compressive strength of

Parameter	R	RS	SL
p_1	0.70	0.60	0.80
p_{5H}	8.00	1.00	8.00
s_2	14.2×10^{-3}	29.9×10^{-3}	11.2×10^{-3}
s_5	1.54×10^{-6}	41.8×10^{-6}	150×10^{-6}
$\varepsilon_{s,cem}$	590×10^{-6}	830×10^{-6}	640×10^{-6}
s_{ef}	−0.51	−0.84	−0.69
$\tau_{s,cem}$	0.027	0.027	0.032
$s_{\tau f}$	0.21	1.55	−1.84

TABLE 4 Parameters of the B4s model for the different cement types: R = normal, RS = rapid hardening, SL = slow hardening.

concrete as an input. It is described by use of the compliance function J (μm/m/MPa), which can be estimated using the following equation:

$$J(t,t_0) = q_1 + J_b(t,t_0) + J_d(t,t_0), \tag{16}$$

in which q_1 (μm/m/MPa) is the asymptotic compliance at loading, J_b (μm/m/MPa) is the basic creep compliance and J_d (μm/m/MPa) is the additional creep compliance due to drying. q_1 is given by:

$$q_1 = \frac{p_1}{E_{cm}}, \tag{17}$$

where p_1 is given in Table 4 and E_{cm} is Young's modulus at 28 days, which can be estimated with:

$$E_{cm} = 4734 \cdot \sqrt{f_{cm}} \tag{18}$$

J_b is decomposed in three terms accounting respectively the aging viscoelastic compliance, the non-aging viscoelastic compliance and the flow compliance:

$$J_b(t,t_0) = q_2 \cdot Q(t,t_0) + q_3 \cdot \ln[1 + (t-t_0)^n] + q_4 \cdot \ln\left(\frac{t}{t_0}\right), \tag{19}$$

with:

$$\begin{cases} q_2 &= s_2 \cdot \left(\frac{f_{cm}}{f_0}\right)^{-1.58} \\ q_3 &= 0.976 \cdot s_2 \cdot \left(\frac{f_{cm}}{f_0}\right)^{-3.19} \\ q_4 &= 4 \times 10^{-3} \cdot \left(\frac{f_{cm}}{f_0}\right)^{-1.16} \end{cases}, \tag{20}$$

where $f_0 = 40$ MPa.

TABLE 5 Values of the aggregate-dependent factor $k_{\tau a}$ for the B4s model.

Aggregate type	$k_{\tau a}$
Diabase	0.06
Quartzite	0.59
Limestone	1.80
Sandstone	2.30
Granite	4.00
Quartz Diorite	15.0

The additional creep compliance due to drying J_d is predicted by using:

$$J_d(t,t_0) = q_5 \cdot \sqrt{|\, e^{-g(t,t_s)} - e^{-g(t_0-t_s)} \,|}, \tag{21}$$

where

$$q_5 = s_5 \cdot \left(\frac{f_{cm}}{f_0}\right)^{-0.45} \cdot \left|k_h \varepsilon_{sh}^{\infty}\right|^{-0.85}, \tag{22}$$

and

$$\begin{cases} k_h &= 1 - h^3 \\ \varepsilon_{sh}^{\infty} &= \varepsilon_s^{\infty} \times 0.57514 \sqrt{\frac{14}{t_0 + \tau_{sh}} + 3} \\ \tau_{sh} &= \tau_0 \cdot k_{\tau a} \cdot (k_s D)^2 \\ \varepsilon_s^{\infty} &= \varepsilon_{s,cem} \cdot \left(\frac{f_{cm}}{f_0}\right)^{s_{ef}} \\ \tau_0 &= \tau_{s,cem} \cdot \left(\frac{f_{cm}}{f_0}\right)^{s_{\tau f}} \end{cases}. \tag{23}$$

D (mm) is the equivalent thickness of the concrete member. The different parameters s_5, $\varepsilon_{s,cem}$, s_{ef}, $\tau_{s,cem}$ and $s_{\tau f}$ are given in Table 4. k_{ta} is the aggregate factor, given

TABLE 6 Values of the shape factor k_s for the B4s model.

Specimen shape	k_s
Infinite slab	1.00
Infinite cylinder	1.15
Infinite square prism	1.25
Sphere	1.30
Cube	1.55

in Table 5 and k_s is the shape factor given in Table 6. h (−) is the relative humidity.

$g(t-t_s)$ determines the speed of drying creep and is given by

$$g(t-t_s)=p_{5H}\cdot\left[1-(1-h)\cdot\tanh\left(\sqrt{\frac{t-t_s}{\tau_{sh}}}\right)\right], \quad (24)$$

where p_{5H} is a parameter given in Table 4.

In this study, the adaptation of the B4s model is done using the same approach in the past to extend the B4 model to account for various types of admixtures and aggregates.[30] This approach takes parameters corresponding to normal hardening cement as reference (R) and introduces new scaling factors to account for the material differences. When they are set equal to one, the original B4s model is recovered.

For basic creep, three scaling factors ζ_1, ζ_2 and ζ_4 are introduced in the definitions of q_1, q_2, q_3 and q_4:

$$\begin{cases} q_1 &= \dfrac{p_1\cdot\zeta_1}{E_{cm}} \\ q_2 &= s_2\cdot\zeta_2\cdot\left(\frac{f_{cm}}{f_0}\right)^{-1.58} \\ q_3 &= 0.976\cdot s_2\cdot\zeta_2\cdot\left(\frac{f_{cm}}{f_0}\right)^{-3.19} \\ q_4 &= 4\times10^{-3}\cdot\zeta_4\cdot\left(\frac{f_{cm}}{f_0}\right)^{-1.16} \end{cases}, \quad (25)$$

ζ_1 adjusts Equation (17) for estimating the initial strain due to the loading. ζ_2 and ζ_4 are scaling parameters for the basic creep model corresponding to early age and late age creep, respectively.

For the drying creep, the optimization was done on J_d against the experimental drying creep compliance J_d^{exp}, defined as the difference between the compliance in unsealed conditions J^{exp} and the compliance in sealed conditions J_b^{exp}, for samples loaded at the same age. Due to the change in Young's modulus between sealed and unsealed samples, the experimental drying creep compliances do not start at zero but show an offset in the range of 2–5 µm/m/MPa. This offset had a non-negligible impact on the calibration of the parameters of the model. For this reason, it was removed for each experiment for the optimization process and the model for drying creep compliance was compared to:

$$J_d^{exp}=J^{exp}(t,t_0,t_s)-J_b^{exp}(t,t_0)-\left[J^{exp}(t_0,t_0,t_s)-J_b^{exp}(t_0,t_0,t_s)\right]. \quad (26)$$

For drying creep the scaling factor ζ_5 is introduced in Equation (22):

$$q_5=s_5\cdot\zeta_5\cdot\left(\frac{f_{cm}}{f_0}\right)^{-0.45}\cdot\left|k_h\varepsilon_{sh}^{\infty}\right|^{-0.85}. \quad (27)$$

3.3 | Calibration method

The calibration is done using the experimental results obtained in this study. It was performed by applying the least squares method on the average of the obtained curves.

To avoid experimental biases at early stage, weights were applied to early stage and late stage results. The experimental results were split into two-time intervals delimited by the transition time t_w. This transition time varied with 11 values logarithmically-spaced between (10^{-3} and 50) days. For each transition time, the weight for the early-stage result ω_1 and the weight for the late-stage result $\omega_2=1-\omega_1$ varied between 20% and 80%. For each calculation, different initial guesses were tested to obtain the parameters that correspond to the global minimum of the objective function written as

$$\mathcal{F}_{obj}(params,t_w)=\begin{aligned}&\omega_1\cdot\left(\mathcal{F}^{model}(params,t\le t_w)\right.\\&\left.-\mathcal{F}^{exp}(t\le t_w)\right)^2+\omega_2\\&\cdot\left(\mathcal{F}^{model}(params,t>t_w)\right.\\&\left.-\mathcal{F}^{exp}(t>t_w)\right)^2,\end{aligned} \quad (28)$$

where $\mathcal{F}^{model}$ is the tested model, $\mathcal{F}^{exp}$ is the experimental result. *params* are the different parameters of the considered model to be calibrated as described in the previous section. The values of the fitted parameters varied at most by 1.5% for different values of weights and transition times in the objective function for all the experiments. The experimental curves were also calibrated without any weights. The results were always in the range of the weighted results. Hence, the results in the following sections correspond to the parameters obtained by performing the calibration without any weights.

4 | RESULTS

In this part, the experimental results of the different mechanical tests are presented. The creep results are expressed in terms of creep compliance J (μm/m/MPa).

4.1 | Experimental Young's modulus and compressive strength results

Table 7 provides Young's modulus and compressive strength according to EN 12390-13.[27] The specimens subjected to drying showed less change in Young's modulus with time and had a lower Young's modulus compared to the sealed samples. As expected, specimens with larger diameters have higher Young's modulus, when exposed to drying. This is coherent with the fact that the drying of samples with larger diameter takes more time.

4.2 | Experimental shrinkage results of AAS concrete

The experimental shrinkage results in both sealed and unsealed conditions are plotted in Figure 2. It can be seen that autogenous shrinkage is high, as already observed in References 23,24. As discussed in a previous study,[3] this could be because of a higher drop in relative humidity during the first days of reaction. As measured in References 31–33, the internal relative humidity of AAS in sealed conditions can drop by 80% after 7 days, while it remains higher than 90% for cement.[34,35] Thus, the capillary pressure in AAS concrete is higher and causes a higher basic shrinkage. Nevertheless, a few authors indicated that the contribution of capillary pressure cannot explain totally basic shrinkage and that other mechanisms should be considered as the reduction of steric-hydration force[33] and creep effects.[36] Moreover, the contribution of drying shrinkage, defined as the difference between experimental results in unsealed conditions and sealed conditions is relatively low in comparison to OPC concrete. For example, in the B3 model,[14,15] only drying shrinkage is taken into account and basic shrinkage is neglected. Thus, the relative humidity gradient between the inside and outside at age of exposure to drying (7 days) is lower for AAS concrete and this leads to lower drying shrinkage.

TABLE 7 Young's modulus and compressive strength results.

Testing age (d)	Exposure age to drying (d)	Diameter (mm)	Young's modulus (GPa)	Compressive strength (MPa)
7	n.a.	100	27.7	40.9
7	n.a.	150	26.7	43.8
28	n.a.	100	30.3	50.4
28	n.a.	150	30.4	57.8
28	7	100	27.7	51.5
28	7	150	29.7	55.8
100	7	100	26.3	56.5

Note: n.a stands for not applicable.

4.3 | Experimental creep results of AAS concrete

The results of basic creep for different specimen diameters and ages are shown in Figure 3. It can be seen that for samples tested in this study, the effect of diameter is not significant on the basic creep behavior of AAS concrete. This is in accordance with the model hypotheses made in both *fib* MC 2010 and B4s models that do not take the notional thickness, and thus the diameter, as a parameter. The initial creep compliance is lower for older samples. This can be explained by the evolution of Young's modulus between both ages (see Table 7). The creep behavior can be discomposed between early-age and late-age deformations. During the first days after applying the load, the specimens loaded at an age of

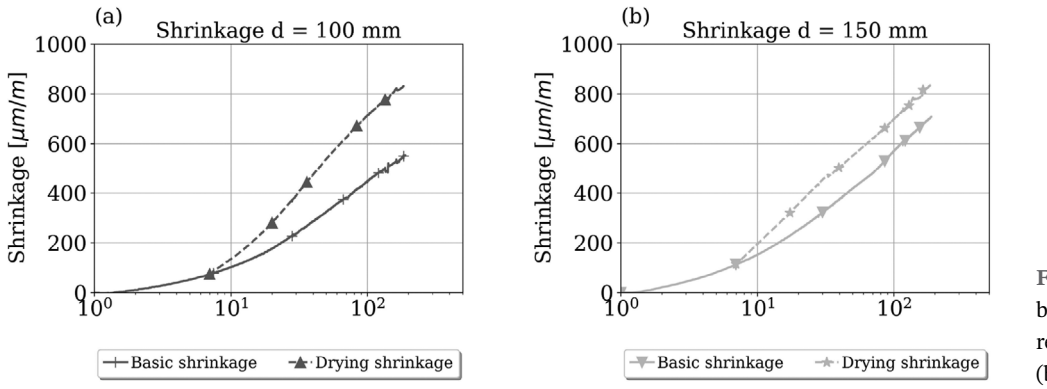

FIGURE 2 Experimental basic and drying shrinkage results (a) for 100 mm diameter (b) for 150 mm diameter.

7 days creep more than the ones loaded at an age of 28 days. This could come from the changes in the microstructure that take place between these ages. Indeed, between 7 and 28 days, as the slag reaction continues, the pore structure becomes denser with smaller pores.[37,38] In particular, at lower degree of reaction, a higher quantity of water in the pore structure is present than after 28 days.[39] This can be put into perspective with the water redistribution in cementitious materials that was observed in Reference 40. The higher water content in the pore structure would induce a higher early-age creep. For the later-age behavior, the rates of creep compliance $L = \frac{dJ}{dt}$ for both 100 and 150 mm diameters and for both loading ages 7 and 28 days are very similar (see Figure 3b). This would support theories that the asymptotic behavior for basic creep depends only on the material as suggested by Vandamme et al.[41] This asymptotic behavior could come from the slipping of C-S-H layers,[42,43] or due to rearrangement of C-S-H, which would result in a reduction of the gel porosity[44] and an increase of the packing density.[41,45] The rate of creep compliance after 100 days for OPC concrete provided in Reference 41 is around 0.05, while it is found to equal 0.13 for AAS in this study. At least two mechanisms could explain the higher creep of AAS. The first one is that the secondary reaction products of AAS are mainly amorphous[46] while portlandite and ettringite, present in OPC concrete as crystalline phases, have a negligible contribution to creep.[47] Hence, with higher amounts of amorphous phases, AAS would creep more. The second explanation could be due to the microstructure of the C-A-S-H gel. Higher uptake of aluminum in the structure, as is the case for AAS in comparison to OPC, increases the amount of bounded water in the C-A-S-H gel.[48] Suwanmaneechot et al.[49] proved that creep increases as the water adsorption thickness increases. For these authors, the mechanism explaining creep is the sliding of C-A-S-H layers. Thus, the higher creep of AAS may be because of more amorphous secondary products and a higher amount of bounded water due to higher aluminum uptake.

The results of drying creep for both 100 and 150 mm diameter specimens are shown in Figure 4. In comparison to basic creep, the creep compliance just after loading for samples loaded at age 7 days is a bit higher (around 2 μm/m/MPa). This comes from the differences in Young's modulus between dried and sealed specimens (see Table 7). As for sealed samples (see Figure 3a), the specimens loaded earlier (i.e., after 7 days) show a much higher increase in compliance from 0 to 10 days (see Figure 4). At later age though, the creep compliance increases much more than the one from sealed samples. The drying creep results for specimens dried after 7 days and loaded after 7, 28 and 100 days, that is, just after drying, 21 days after the start of drying and 93 days after the start of drying, respectively, are shown in Figure 5. It can be seen that the different samples loaded after 7, 28 or 100 days show the same increase in compliance between 10 days and 84 days of loading. In Reference 3 it was already pointed out that the internal drying of AAS is much higher than the one of OPC and that the internal relative humidity drops lower than 85% after 7 days.[33] This means that the moisture gradient with the ambient environment is lower for AAS concrete and that the drying of AAS concrete specimens should be lower than for OPC systems. This would also explain why the difference in drying creep between 100 mm diameter specimens and 150 mm diameter specimens is very low (less than 5 μm/m/MPa after 100 days for loadings at either 7 or 28 days).

The influence of the ratio R_{cr} on creep compliance is plotted in Figure 6 (a). The creep behavior of the sample loaded at 20% of the compressive strength at 28 days $f_{cm,28}$ is very similar to the one loaded at 33% of $f_{cm,28}$. The sample loaded at 60% of $f_{cm,28}$ tends to show higher creep compliance. Such higher creep strains for higher loading have already been reported in the literature for OPC and are explained by the increased formation of microcracks.[50,51] Zhou et al.[21] in past have pointed out that R_{cr} is found to have little influence on the creep coefficient for AAS concrete, which is also evident from

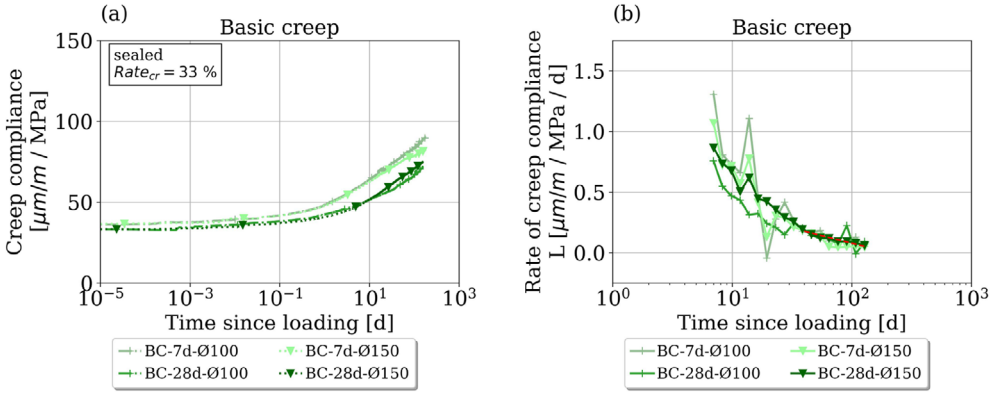

FIGURE 3 Experimental basic creep results for sustained loading from 7 or 28 days with 100 or 150 mm diameters. (a) Creep compliance (b) Rate of creep compliance. On (b) the red line is plotted only to guide the eye.

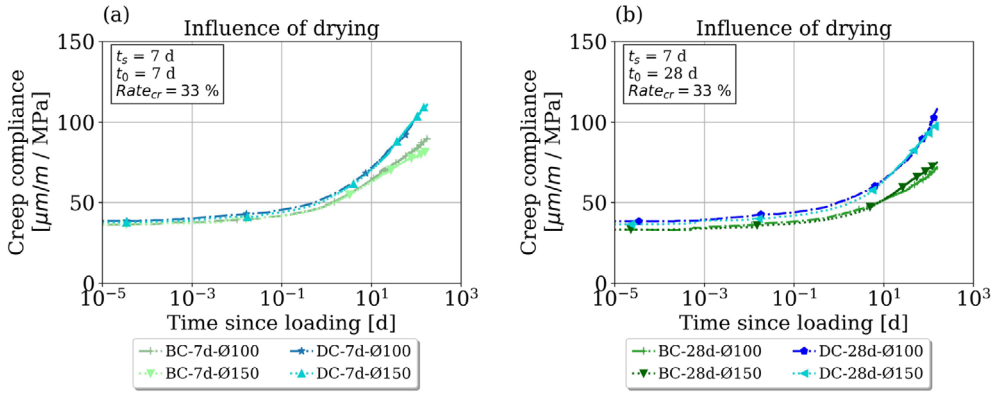

FIGURE 4 Experimental drying creep measured for age of exposure to drying t_s equal to 7 days and loading at ages (a) 7 or (b) 28 days.

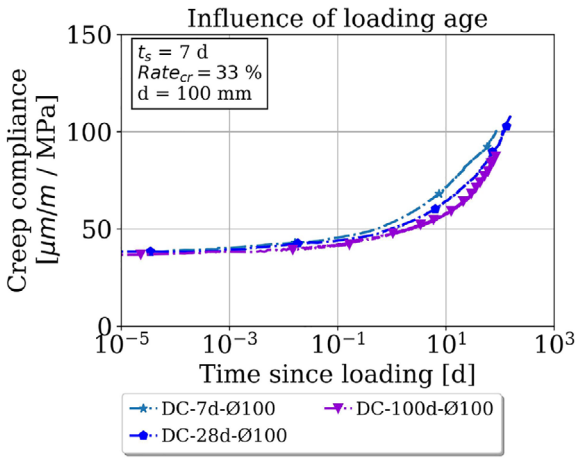

FIGURE 5 Experimental drying creep measured for samples dried from 7 days and loaded at different ages (7, 28 and 100 days).

experimental results from this study as shown in Figure 6 (b). This would mean that despite a higher number of microcracks with higher loads, the creep strain remains linear with R_{cr} up to 60% of the compressive strength. This is contradictory to assumptions made for OPC-based concrete in *fib* MC 2010[52] and B4s model,[30] where the linearity between creep strain and applied load is assumed to be 40% and 45% of the compressive strength, respectively.

5 | CALIBRATION OF CREEP RESULTS FOR AAS WITH EXISTING ENGINEERING MODELS

5.1 | Calibration of creep results for AAS concrete with the *fib* MC 2010

As presented in Section 3, the creep behavior is expressed with the creep coefficient ϕ_{cc} for the *fib* MC 2010. The basic creep coefficient ϕ_{bc} is used for basic creep (Equation 7), while the drying creep coefficient ϕ_{dc} is used for drying creep (Equation 9).

5.1.1 | Calibration of the basic creep results with the *fib* MC 2010

The basic creep model from the *fib* MC 2010 is calibrated for AAS concrete from the results of the specimens BC-7d-Ø100, BC-7d-Ø150, BC-28d-Ø100 and BC-28d-Ø150. The results of the calibration of the *fib* MC 2010 with the Equation (13) are shown in Figure 7 and the calibrated parameters are summarized in Table 8. The original *fib* MC 2010 underestimates the value of the basic creep coefficient by at least factor two. The calibrated extended *fib* MC 2010 as described in Section 3 (Equation 13) underestimates the creep coefficient at early ages. However, at later age, the proposed model is able to capture the basic creep behavior of concrete. The results with the use of the Equation (15) for the calibration for β_{bc} are also given in Figure 7 and Table 8. As expected, the modeled creep coefficient does not start at 0 in comparison to Equation (13). However, the proposed model fits correctly the experimental curves after 10 days of loading. In this case, $\xi_{bc,1}$ characterizes the asymptotic behavior and is in the range (1.7–2.3). The coefficient $\xi_{bc,2}$ is in the range (1.1–1.7) and indicates that the kinetics of creep for AAS concrete is slower than the one of cement.

5.1.2 | Calibration of the drying creep results with the *fib* MC 2010

For drying creep, the calibration was done using the creep results of the samples DC-7d-Ø100, DC-7d-Ø150, DC-28d-Ø100 and DC-28d-Ø150. The use of the equation (Equation 13) with the calibration method presented in Section 3.3 did not allow the convergence of the

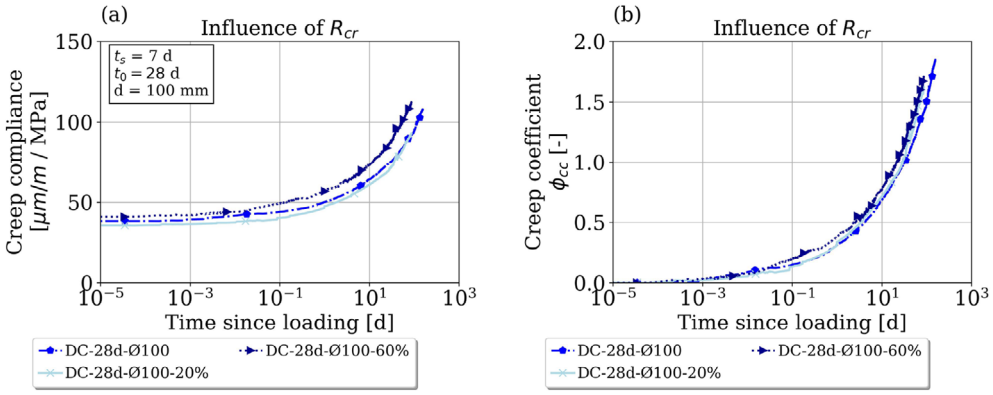

FIGURE 6 Experimental drying creep for samples dried after 7 days and loaded at 28 days at different sustained loads. (a) Creep compliance (b) Creep coefficient.

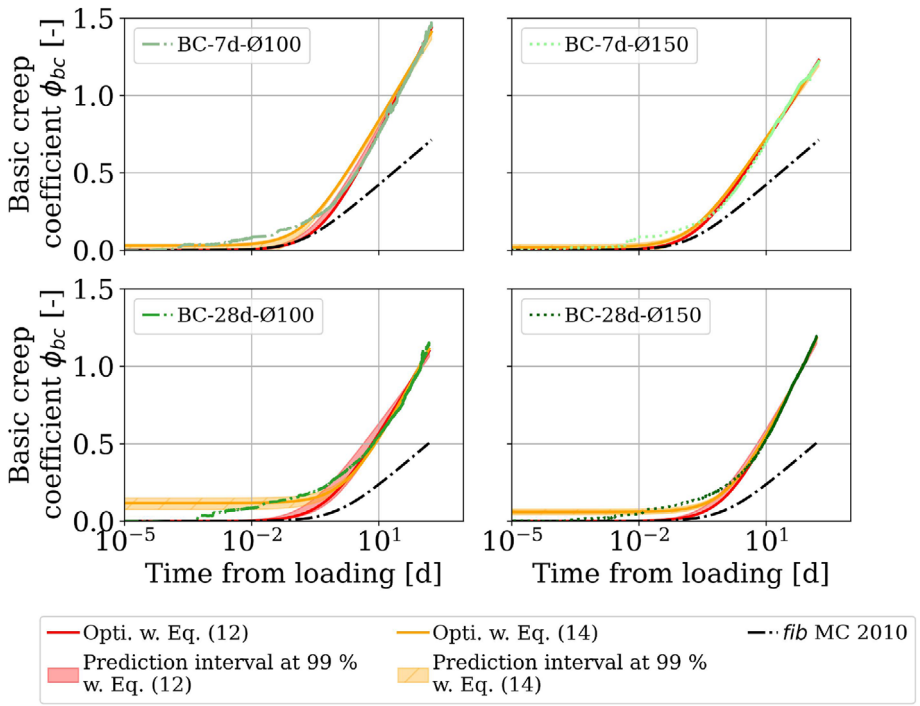

FIGURE 7 Calibration of the basic creep model of the *fib* MC 2010 from experimental results obtained in this study. Calibration is made with both Equations (13) and (15) independently. The prediction intervals correspond to changes in the calibrated parameters from changes in the optimization weights at early stage and late stage.

TABLE 8 Results of the calibration for basic creep with the *fib* MC 2010.

Model Name	Equation (13)		Equation (15)	
	$\xi_{bc,1}$	$\xi_{bc,2}$	$\xi_{bc,1}$	$\xi_{bc,2}$
BC-7d-Ø100	2.37	2.80	1.98	1.15
BC-7d-Ø150	1.81	1.40	1.71	1.11
BC-28d-Ø100	1.96	0.57	2.20	1.68
BC-28d-Ø150	2.39	1.12	2.33	1.28

optimization process, despite trials with several weights and transition times between early-age and late-age. The comparison between the drying creep coefficients ϕ_{dc} from the experiments and the one predicted by the original *fib* MC 2010 are plotted in Figure 8.

At early-age, as explained in Section 4.3, the difference in the creep evolution between sealed and unsealed samples is quite low, resulting in a low drying creep. Up to around 10 days, the drying creep coefficient ϕ_{dc} is overestimated by the *fib* MC 2010. However, after 10 days, the evolution of ϕ_{dc} reaches an asymptotic behavior with a slope higher than predicted by the *fib* MC 2010. These results raise a possible issue on the adaptability of the *fib* MC 2010 to describe the drying creep of AAS with the Equation (8).

In conclusion, the basic creep model of the *fib* MC 2010 can be extended for AAS concrete. After 100 days, the basic creep coefficient is around two times higher for such concrete. For drying creep though, the *fib* MC 2010 could not be adapted with the method proposed in Reference 17.

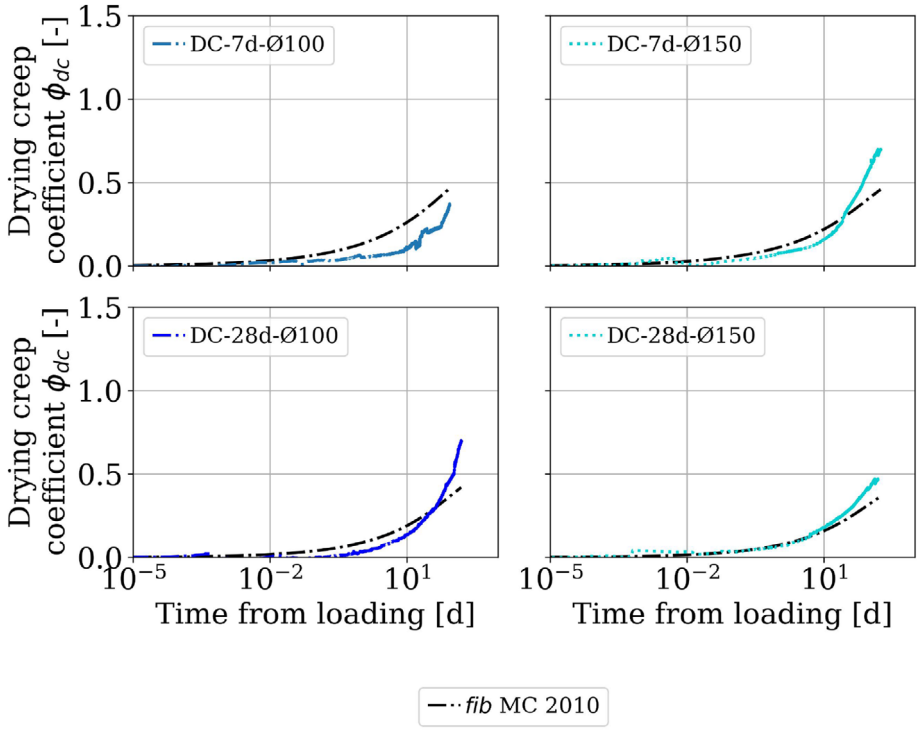

FIGURE 8 Comparison of the drying creep coefficient ϕ_{dc} modeled with the *fib* MC 2010 with the experimental results obtained in this study.

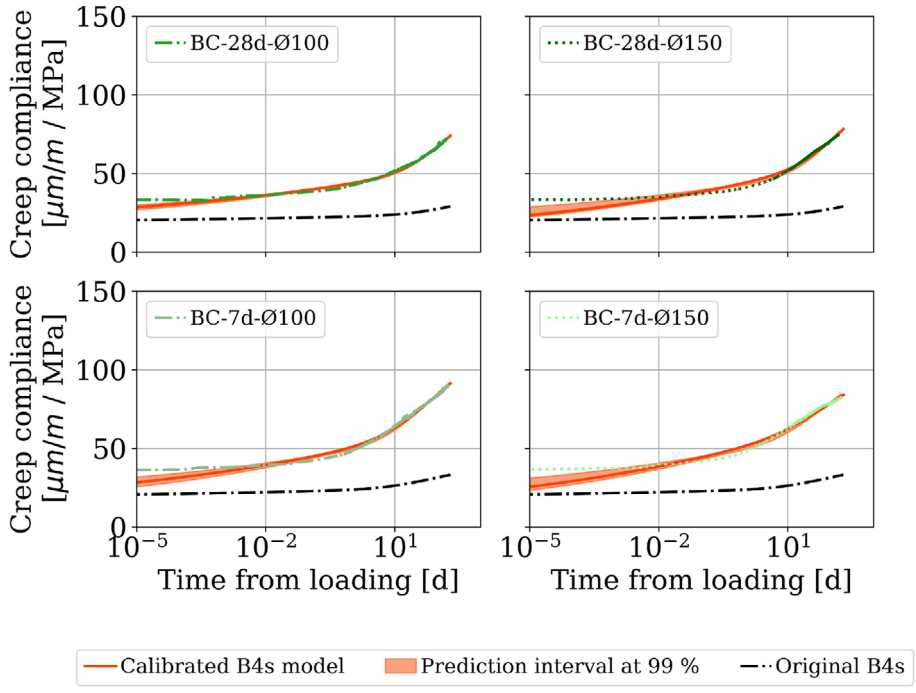

FIGURE 9 Calibration of the basic creep model of the B4s model from experimental results obtained in this study. The prediction interval corresponds to changes in the calibrated parameters from changes in the optimization weights at early stage and late stage.

5.2 | Calibration of creep results for AAS concrete with the B4s model

In the B4s model, the creep behavior is described mathematically by the compliance function, as presented in Section 3 (Equation 16).

5.2.1 | Calibration of the basic creep results with the B4s model

The calibration of the basic creep behavior with the B4s model is plotted in Figure 9 and the corresponding obtained parameters are given in Table 9. The values of

ζ_1 are lower than 1 meaning that the elastic strain due to the initial loading is lower than predicted by the original B4s model. Conversely, the values of ζ_2 are in the range 7–9 indicating that the strain evolution after the loading is relatively higher than for OPC concrete. This indicates that AAS concrete creeps much more in the first hours of loading, in comparison with cement-based systems. The same conclusion could be drawn with an alternative optimization approach where ζ_1 was fixed to 1. In this case, ζ_2 varied between 4.8 and 5.5. For the creep behavior at later-age, ζ_4 values go from 2.24 to 4.01. It means that the creep evolution at late-age is higher than predicted by the B4s model, as was the case for *fib* MC 2010 model. Similar to the *fib* MC 2010, the B4s model can be adapted to describe qualitatively the basic creep behavior of AAS concrete despite much higher values of basic creep.

5.2.2 | Calibration of the drying creep results with the B4s model

As seen in Figure 10, the original B4s model overestimates the drying creep behavior for AAS concrete at the initial stage. However, the appropriate calibration of ζ_5 from Equation (27) provides satisfactory results with the B4s model. The low values of the calibrated parameter ζ_5 (see Table 10) reflect that drying creep is lower in the case of AAS concrete compared to OPC concrete. The lower drying creep for AAS concrete can be attributed to the relatively low external drying due to the relatively low internal humidity of AAS concrete, as explained in Section 4.3.

It should be noted that in comparison to Reference 24, the experimental results of this study did not reach the second part of the characteristic S-curve for creep behavior. This could influence the optimization of ζ_5. For this reason, the results of Table 10 should be referred to with caution.

In conclusion, the B4s model can be extended for AAS concrete for both basic creep and drying creep. The basic creep compliance should be multiplied by a factor between two and three after 100 days. In drying conditions, the extended B4s model describes correctly the creep evolution. Given that the functional forms of the B4s model are based on the solidification theory,[30]

TABLE 9 Results of the calibration for basic creep with the B4s model.

Name	ζ_1	ζ_2	ζ_4
BC-7d-Ø100	0.75	8.1	3.5
BC-7d-Ø150	0.47	9.5	2.2
BC-28d-Ø100	0.98	7.2	4.0
BC-28d-Ø150	0.53	9.7	4.1

TABLE 10 Results of the calibration for drying creep with the B4s model.

Name	ζ_5
DC-7d-Ø100	0.26
DC-7d-Ø150	0.54
DC-28d-Ø100	0.48
DC-28d-Ø150	0.50

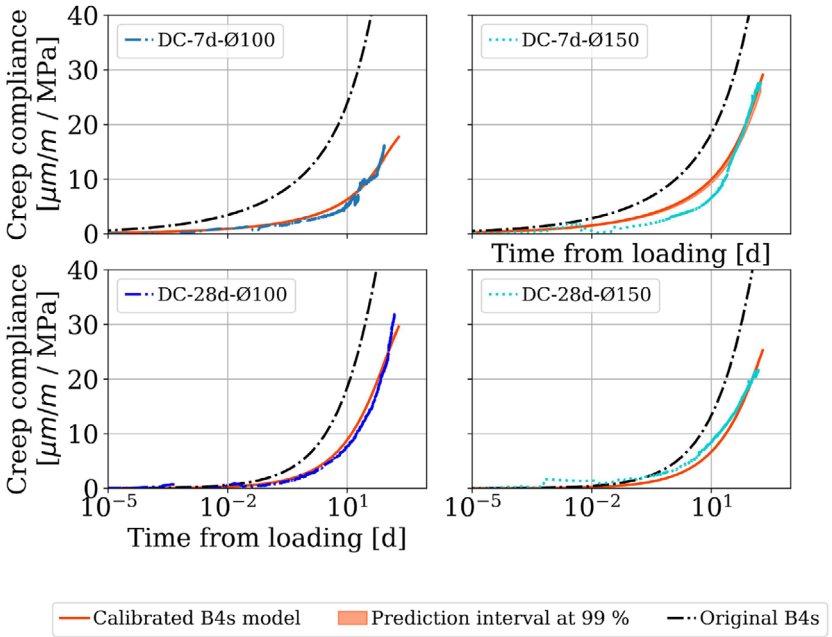

FIGURE 10 Calibration of the additional part of the creep compliance due to drying of the B4s model from the experimental results obtained in this study. The prediction interval corresponds to changes in the calibrated parameters from changes in the optimization weights at early stage and late stage.

this theory could be used in the future to understand the creep behavior of AAS concrete.

6 | CONCLUSION

In this study, new experimental results are presented on the creep of AAS for both sealed and unsealed conditions. The following conclusions can be drawn from this study:

- In comparison to OPC concrete, basic creep is around two times higher after 100 days of loading. The rate of basic creep compliance at late age is also higher for AAS concrete.
- The drying creep of AAS concrete is less significant for AAS concrete for both diameters 100 and 150 mm. It is notably lower than OPC concrete at early-age and this could be explained by a higher internal drying during the chemical reaction between the slag and the alkali solution.
- The linearity of the creep strain with the applied load is valid up to at least 60% of the compressive strength for AAS, while the linearity range is limited to 45% for OPC.
- Both *fib* MC 2010 and B4s models were calibrated from the experimental results presented in this study. Both models could be extended for basic creep. The scaled parameters indicate that AAS concrete creeps around two times more than OPC concrete and that the basic creep rate at late-age is higher.
- For drying creep, the *fib* MC 2010 fails to capture the experimental trend by a simple adaptation of the existing model. A new form function for drying creep would be required to extend the model to AAS concrete. On the contrary, the B4s model was able to correctly capture the drying creep evolution. The scaling factor shows that the drying creep compliance is around two times lower than for OPC concrete.

The above conclusions are subjective to the mix tested in this study. Further studies would be required in the future for varied mix designs and different activator solutions to come up with the appropriate extension of engineering models for AAS concrete.

ACKNOWLEDGMENTS

The project leading to this application has received funding from the European Union's Horizon 2020 research and innovation program under the Marie Skłodowska-Curie grant agreement No 813596. Open Access funding enabled and organized by Projekt DEAL.

CONFLICT OF INTEREST STATEMENT

The authors declare that they have no conflict of interest.

DATA AVAILABILITY STATEMENT

The data that support the findings of this study are available from the corresponding author upon reasonable request.

ORCID

Richard Caron https://orcid.org/0000-0002-5741-6440

REFERENCES

1. Provis JL. Geopolymers and other alkali activated materials: why, how, and what? Mater Struct. 2014;47(1–2):11–25.
2. Garcia-Lodeiro I, Palomo A, Fernández-Jiménez A. 2 - an overview of the chemistry of alkali-activated cement-based binders. In: Pacheco-Torgal F, Labrincha JA, Leonelli C, Palomo A, Chindaprasirt P, editors. Handbook of alkali-activated cements, mortars and concretes. Oxford: Woodhead Publishing; 2015. p. 19–47. https://www.sciencedirect.com/science/article/pii/B9781782422761500022
3. Caron R, Patel RA, Dehn F. Extension of the fib MC 2010 for basic and dryings hrinkage of alkali–activated slag concretes. Struct Concr. 2022;64(48):106107.
4. Fernández-Jiménez A, Puertas F. Structure of calcium silicate hydrates formed in alkaline-activated slag: influence of the type of alkaline activator. J Am Ceram Soc. 2003;86(8):1389–94.
5. Provis JL, Arbi K, Bernal SA, Bondar D, Buchwald A, Castel A, et al. RILEM TC 247-DTA round robin test: mix design and reproducibility of compressive strength of alkali-activated concretes. Mater Struct. 2019;52(5):3683.
6. Komljenović MM, Baščarević Z, Marjanović N, Nikolić V. Decalcification resistance of alkali-activated slag. J Hazard Mater. 2012;233-234:112–21.
7. Komljenović M, Baščarević Z, Marjanović N, Nikolić V. External sulfate attack on alkali-activated slag. Constr Build Mater. 2013;49(7):31–9.
8. Sellin JP, Barthélémy JF, Bondonet G, Cauvin B, Torrenti JM. Delayed deformations of concrete structures: The Savines bridge and the Cheviré bridge. 2015.
9. Bažant ZP, Hon M, Yu Q, Li G-H. Excessive long-time deflections of prestressed box girders. I: record-span bridge in Palau and other paradigms. J Struct Eng. 2012;138:6.
10. Song HW, Kim SH, Byun KJ, Song YC. Creep prediction of concrete for reactor containment structures. Nucl Eng Des. 2002;09(217):225–36.
11. Lundqvist P, Nilsson LO. Evaluation of prestress losses in nuclear reactor containments. Nucl Eng Des. 2011;241(1):168–76.
12. Liu Z, van den Heede P, de Belie N. Effect of the mechanical load on the carbonation of concrete: a review of the underlying mechanisms, test methods, and results. Materials. 2021;14(16):4407.
13. Fu C, Ye H, Jin N, Huang Y. Chloride penetration in reinforced concrete beams under combined sustained loading and drying–wetting cycles. J Mater Civ Eng. 2020;32(4):602.
14. Bazant ZP, Baweja S. Creep and shrinkage prediction model for analysis and design of concrete structures— Model B^3. Mater Struct. 1995;28:357–65.
15. Bazant ZP, Baweja S. Creep and shrinkage prediction model for analysis and design of concrete structures: Model B3. In:

Al-Manaseer A, editor. Adam neville symposium: creep and shrinkage—structural design effects; ACI SP–194. Michigan: American Concrete Institute, Farmington Hills; 2000. p. 1–83.
16. Wendner R, Hubler MH, Bažant ZP. Optimization method, choice of form and uncertainty quantification of model B4 using laboratory and multi-decade bridge databases. Mater Struct. 2015;48(4):771–96.
17. Tošić N, de La Fuente A, Marinković S. Creep of recycled aggregate concrete: experimental database and creep prediction model according to the fib model code 2010. Constr Build Mater. 2019;195:590–9.
18. Wallah S, Rangan B. Low-calcium fly ash-based geopolymer concrete: long term properties. Perth, Australia: Curtin Research Publications. Curtin University of Technology; 2006.
19. Sagoe-Crentsil K, Brown T, Taylor A. Drying shrinkage and creep performance of geopolymer concrete. J Sustainable Cem-Based Mater. 2013;2(1):35–42.
20. Castel A, Foster SJ, Ng T, Sanjayan JG, Gilbert RI. Creep and drying shrinkage of a blended slag and low calcium fly ash geopolymer concrete. Mater Struct. 2016;49(5):1619–28.
21. Zhou X, Wang Y, Zheng W, Chen P, Zeng Y. Effect of stress–strength Ratioon creep property of sodium silicate–based alkali-activated slag concrete. Appl Sci. 2019;9(18):3643.
22. Un CH, Sanjayan JG, San Nicolas R, van Deventer JSJ. Predictions of long-term deflection of geopolymer concrete beams. Constr Build Mater. 2015;94(7):10–9.
23. Ma J, Dehn F. Shrinkage and creep behavior of an alkali-activated slag concrete. Struct Concr. 2017;18(5):801–10.
24. Humad AM, Provis JL, Habermehl-Cwirzen K, Rajczakowska M, Cwirzen A. Creep and long-term properties of alkali-activated Swedish-slag concrete. J Mater Civ Eng. 2021;33(2):635.
25. Provis JL, Winnefeld F. Outcomes of the round robin tests of RILEM TC 247-DTA on the durability of alkali-activated concrete. MATECWeb Conf. 2018;199:02024.
26. DIN EN 12390-3. Prüfung von Festbeton – Teil 3: Druckfestigkeit von Probekörpern; Deutsche Fassung EN 12390-3:2019. Beuth Verlag 2019.
27. DIN EN 12390-13. Prüfung von Festbeton – Teil 13: Bestimmung des Elastizitätsmoduls unter Druckbelastung(Sekantenmodul); Deutsche und Englische Fassung prEN 12390-13:2019. Beuth Verlag 2019.
28. PT1prEN1992-1-1. Eurocode 2: design of concrete structures: part 1–1: general rules and rules for buildings, bridges and civil engineering structures. Brussels: CEN; 2017.
29. Tošić N, de La Fuente A, Marinković S. Shrinkage of recycle daggregate concrete: experimental database and application of fib model code 2010. Mater Struct. 2018;51(5):125.
30. RILEM draft recommendation: TC-242-MDC multi-decade creep and shrinkage of concrete: material model and structural analysis*. Mater Struct. 2015;48(4):753–70.
31. Song C, Choi YC, Choi S. Effect of internal curing by superabsorbent polymers – internal relative humidity and autogenous shrinkage of alkali-activated slag mortars. Constr Build Mater. 2016;123(10):198–206.
32. Jia Z, Yang Y, Yang L, Zhang Y, Sun Z. Hydration products, internal relative humidity and drying shrinkage of alkali activated slag mortar with expansion agents. Constr Build Mater. 2018;158(2):198–207.
33. LiZ LT, Liang X, Dong H, Ye G. Mechanisms of autogenous shrinkage of alkali-activated slag and fly ash pastes. Cem Concr Res. 2020;135:106107.
34. Jensen OM, Hansen PF. Autogenous relative humidity change in silica fume-modified cement paste. Adv Cem Res. 1995;7(25):33–8.
35. Lura P, Jensen OM, van Breugel K. Autogenous shrinkage in high-performance cement paste: an evaluation of basic mechanisms. Cem Concr Res. 2003;33:223–32.
36. Abate SY, Park S, Kim H-K. Parametric modeling of autogenous shrinkage of sodium silicate-activated slag. Constr Build Mater. 2020;262:120747. https://www.sciencedirect.com/science/article/pii/S0950061820327525
37. Collins F, Sanjayan JG. Effect of pore size distribution on drying shrinkage of alkali-activated slag concrete. Cem Concr Res. 2000;30:1401–6.
38. Gruskovnjak A, Lothenbach B, Holzer L, Figi R, Winnefeld F. Hydration of alkali-activated slag: comparison with ordinary Portland cement. Adv Cem Res. 2006;18(3):119–28.
39. Ye H, Radlińska A. Quantitative analysis of phase assemblage and chemical shrinkage of alkali-activated slag. J Adv Concr Technol. 2016;14(5):245–60.
40. Wyrzykowski M, Mcdonald P, Scrivener K, Lura P. Water redistribution within the microstructure of cementitious materials due to temperature changes studied with 1 H NMR. J Phys Chem C. 2017;11(121):27950–62.
41. Vandamme M, Ulm FJ. Nanoindentation investigation of creep properties of calcium silicate hydrates. Cem Concr Res. 2013;52:38–52.
42. Feldman RF. Mechanism of creep of hydrated Portland cement paste. Cem Concr Res. 1972;2:521–40.
43. Vichit-Vadakan W, Scherer G. Beam-bending method for permeability and creep characterization of cement paste and mortar. Proceedings of the 6th international conference on creep, shrinkage and durability mechanics of concrete and other quasi-brittle materials. Cambridge, MA: Elsevier; 2001. p. 27–32.
44. Thomas JJ, Jennings HM. A colloidal interpretation of chemical aging of the C-S-H gel and its effects on the properties of cement paste. Cem Concr Res. 2006;36:30–8.
45. Haist M, Divoux T, Krakowiak KJ, Skibsted J, Pellenq RJM, Müller HS, et al. Creep in reactive colloidal gels: a nanomechanical study of cement hydrates. Phys Rev Res. 2021;3(4):68.
46. Jae Eun O, Monteiro PJM, Jun SS, Choi S, Clark SM. The evolution of strength and crystalline phases for alkali-activated ground blast furnace slag and fly ash-based geopolymers. Cem Concr Res. 2010;40(2):189–96.
47. Li J, ZhangW MPJM. Preferred orientation of calcium aluminosilicate hydrate compacts: implications for creep and indentation. Cem Concr Res. 2021;143(33):106371.
48. Kapeluszna E, Kotwica Ł, Różycka A, Gołek Ł. Incorporation of Al in C-A-S-H gels with various Ca/Si and Al/Si ratio: microstructural and structural characteristics with DTA/TG, XRD, FTIR and TEM analysis. Constr Build Mater. 2017;155:643–53.

49. Suwanmaneechot P, Aili A, Maruyama I. Creep behavior of C-S-H under different drying relative humidities: interpretation of microindentation tests and sorption measurements by multi-scale analysis. Cem Concr Res. 2020;132(1):106036.
50. Rossi P, Tailhan JL, Le Maou F, Gaillet L, Martin E. Basic creep behavior of concretes investigation of the physical mechanisms by using acoustic emission. Cem Concr Res. 2012;42(1):61–73.
51. Tasevski D, Ruiz MF, Muttoni A. Analogy between sustained loading and strain rate effects on the nonlinear creep response of concrete. In: Hellmich C, Pichler B, Kollegger J, editors. Concreep 10. Reston, VA: American Society of Civil Engineers; 2015. p. 1187–93.
52. FIB. *fib* model code for concrete structures 2010. Lausanne: International Federation for Structural Concrete (fib); 2013.

AUTHOR BIOGRAPHIES

Richard Caron, Institute of Building Materials and Concrete Structures, Karlsruhe Institute of Technology (KIT), 76131 Germany. Email: richard.caron@kit.edu.

Ravi A. Patel, Institute of Building Materials and Concrete Structures, Karlsruhe Institute of Technology (KIT), 76131 Germany. Email: ravi.patel@kit.edu.

Frank Dehn, Institute of Building Materials and Concrete Structures, Karlsruhe Institute of Technology (KIT), 76131 Germany. Email: frank.dehn@kit.edu.

How to cite this article: Caron R, Patel RA, Dehn F. Experimental study on basic and drying creep for an alkali-activated slag concrete and comparison with existing creep models. Structural Concrete. 2023. https://doi.org/10.1002/suco.202300134